Journal of Materials Chemistry A

ROYAL SOCIETY OF CHEMISTRY

PAPER

View Article Online
View Journal | View Issue

Cite this: J. Mater. Chem. A, 2023, 11, 9829

Biomass-derived two-dimensional N,O-doped carbon with embedded binary-metal nanoparticles enables dendrite-free potassium-metal anodes†

Qing Shen, Yibo He and Junjie Wang *

Potassium metal batteries (PMBs) are expected to become the most promising new generation of new type large-scale energy storage equipment owing to their abundant resources, low cost, and low operating potential. However, the direct use of metallic potassium (K), especially the "hostless" K metal, leads to easy growth of dendrites that pierce the separator, resulting in a short circuit of the battery. In this work, a simple and effective strategy to construct dendrite-free PMBs *via* plating metallic K into binary-metal (NiCo, NiFe, CoFe) nanoparticle-embedded two-dimensional (2D) N,O co-doped carbon (K–NiCo@NOGC, K–NiFe@NOGC, K–CoFe@NOGC) was proposed. The factors affecting the electrochemical performance of potassium metal cells were discussed from the aspects of experiment and theoretical calculation. Our fundamental studies reveal that potassium dendrite growth can be effectively inhibited on the substrate containing nitrogen-oxygen rich functional groups, as confirmed by low nucleation overpotential, high coulombic efficiency and enhanced adsorption energy. Among the three kinds of synthesized materials, NiCo@NOGC can serve as an ideal host for dendrite-free potassium deposition and exhibits outstanding stable cycling performance with high coulombic efficiency (CE) at a current density of 0.5 mA cm^{-2} (CE = 99.4% after 450 cycles). Moreover, the practicality and functionality of this anode are demonstrated by assembling K–NiCo@NOGC||PB full batteries with a long cycle life of 500 cycles and a high-capacity retention of 80%.

Received 15th February 2023
Accepted 18th April 2023

DOI: 10.1039/d3ta00904a

rsc.li/materials-a

1 Introduction

Under the influence of the concept of sustainable development, human society is paying growing attention to environmental issues, and the desire for clean energy is increasing.[1–3] With the popularization of electric vehicles and the development of large-scale energy storage, conventional lithium-ion batteries (LIBs) (with an energy density of about 250 W h kg^{-1}) with graphite as an anode material (372 mA h g^{-1}) have gradually been unable to meet the market demand.[4–8] And with the continuous increase in the market share of electric vehicles, the demand for lithium metal is also growing rapidly. Nevertheless, the limited lithium resources, uneven distribution, and high mining costs have led to the continuous increase in the price of lithium-ion batteries, which may severely restrict their larger-scale applications in the future.[9–11] Fortunately, as an alkali metal with similar chemical properties to lithium, potassium (K) has much more natural reserves than lithium.[12,13] In addition, potassium metal anodes have a higher theoretical specific capacity (687 mA h g^{-1})[14,15] compared with traditional anode materials. Meanwhile, the redox potential K/K^+ of potassium (−2.93 V compared to the standard hydrogen electrode) is lower than that of Na/Na^+ (−2.71 V) and closer to that of Li/Li^+(−3.04 V).[16] Besides, the potassium metal anode can also be matched with the potassium-free cathode to form a full battery (K–O_2, K–CO_2, K–S, K–organic).[17] These properties guarantee a high ionic mobility, a high conductivity, and a high energy density of a K-metal full cell.[11] Therefore, potassium metal batteries (PMBs) are expected to become a new generation of new type large-scale energy storage equipment.

However, it is extremely difficult to use K metal directly as an anode in reversible plating and stripping processes. Potassium metal is known to be highly reactive and will spontaneously react with the electrolyte to form a solid electrolyte interface (SEI) layer.[18,19] In addition, due to the "hostless" nature of K-metal anodes, the SEI is unstable and can be extremely easily disrupted by a mechanical deformation during the process of K plating/stripping.[20] Previous studies have found that the formation of a repeatedly unstable SEI during K plating/stripping can hardly withstand large electrode volume fluctuations, which further promotes the growth of K dendrites.[21,22] Furthermore, non-uniform current flow and potassium ion flux "hostless" K metal anodes lead to inhomogeneous nucleation,

State Key Laboratory of Solidification Processing, School of Materials Science and Engineering, Northwestern Polytechnical University, Xi'an, Shaanxi 710072, People's Republic of China. E-mail: wang.junjie@nwpu.edu.cn

† Electronic supplementary information (ESI) available: Experimental section, XRD patterns, SEM and TEM figures, XPS spectra, electrochemical results and EIS spectra (Fig. S1–S16). See DOI: https://doi.org/10.1039/d3ta00904a

which makes K morphology uncontrollable and causes the growth of K dendrites.[23,24] With the growth of dendritic K, the protruding K dendrites can easily penetrate the separator, causing the cell to short circuit.[25,26] These problems must be overcome in order to advance the research and application of K-metal batteries. While there are some reports of work on how to inhibit potassium dendrite growth, research in this area is still in its early stages.

Very recently, several effective protocols have been reported to reduce the depletion of K and inhibit dendrite growth, such as modifying the electrolyte composition,[27,28] introducing an artificial solid-electrolyte interphase (ASEI),[29] and substituting the metal anode with a liquid Na–K alloy.[17,30] Nevertheless, electrolyte modification and ASEI cannot repress the huge volumetric change during K plating/stripping, and the employment of liquid K–Na alloy anodes may lead to serious safety hazards. Recently, potassium was hosted within 3D scaffolds to homogenize K^+ influx and to minimize the volume change. In particular, the passivation of the potassium metal surface by 2D materials has attracted recent attention by enabling stable K electrode-position and suppressed dendrite formation.[31-33] However, the direct use of 2D materials to protect the surface of K anodes remains challenging because such materials have poor affinity for potassium metal, leading to high nucleation barriers and uneven potassium deposition. Although, in recent studies, different groups have introduced 2D carbon frameworks containing lithiophilic metal nanoparticles (Co, Fe and Ni) to guide homogeneous initial Li deposition,[34-37] such methods have not been reported for potassium metal batteries. In addition, much of the reported fabrication of metal-embedded carbon structures requires a complex top-down process, which is usually unsuitable for large-scale electrode production in the field of metal cells.[38,39]

Therefore, in this work we developed bimetal nanoparticle (NiCo, NiFe, CoFe) embedded 2D N,O-codoped graphited carbon (denoted as NiCo@NOGC, NiFe@NOGC, CoFe@NOGC) synthesized by a simple process of hydrothermal and annealing with uniformly distributed potassium-philic functional groups on the surface as a robust nucleation buffer layer of PMBs. Electrochemical measurements confirmed that the NiCo@NOGC coated copper collector exhibits excellent electrochemical performance with a low nucleation overpotential, small voltage hysteresis, and high coulombic efficiency (CE). Besides, the K–NiCo@NOGC composite anode exhibits better cycling stability and rate performance than pristine K in full battery systems with the Prussian blue (PB) cathode. This study revealed the following mechanisms: first, co-doping of N and O in the carbon matrix enhanced the affinity between K and the substrate, resulting in smooth nucleation of K as well as a uniform deposition process; Second, the 2D carbon network with a high surface provides sufficient space to suppress the volume change during K plating/stripping. Finally, both the 2D graphitized carbon network and the highly dispersed NiCo alloy nanoparticles can guide the uniform dispersion of electrons to avoid charge concentration, further restraining the growth of K dendrites and maintaining long-term cycling stability.

2 Results and discussion

2.1. Structural characterization of the NiCo@NOGC composite

The NiCo@NOGC composite was first prepared with conventional hydrothermal and pyrolysis methods as illustrated in Fig. 1(a). Plant leaves are known to be rich in carbon, nitrogen, and oxygen because they are composed of protein, plant fiber, lipids, sugar, starch, and vitamins.[40] Therefore, a two-dimensional nitrogen and oxygen co-doped carbon matrix (N, O–C) was obtained by a simple hydrothermal method using leaves as the original material. Then, the NiCo@NOGC precursor was synthesized using N, O–C, $Co(NO_3)_2 \cdot 6H_2O$, and $Ni(NO_3)_2 \cdot 6H_2O$ under solvothermal conditions. After high-temperature pyrolysis, a product in which NiCo alloy nanoparticles are uniformly dispersed in a nitrogen and oxygen-rich 2D graphited carbon layer was obtained (Fig. 1(b) and (c)). This can be attributed to the combination of nickel and cobalt atoms to form bimetallic NiCo alloy nanoparticles, and their raw materials bring more nitrogen and oxygen. Furthermore, the N, O–C self-crosslinking transformed the N, O-rich 2D graphitized carbon layers with functional group surfaces due to the long-distance interaction between carbon blocks and functional groups induced between adjacent N and O–C, whereas metallic cobalt and nickel can promote the graphitization of carbon during pyrolysis.[41] TEM measurement of NiCo@NOGC (Fig. 1(c)) revealed that the average size of NiCo alloy nanoparticles dispersed in NiCo@NOGC is around 8.8 nm. And the clear lattice fringes with interplanar distances of 0.202 and 0.179 nm were measured using TEM at a high resolution of 5 nm, which correspond to the inter-planar distances of (111) and (200) planes of the NiCo alloy, respectively (Fig. 1(d)). In addition, elemental mapping analysis demonstrated a uniform distribution of C, N, O, Ni and Co elements in NiCo@NOGC, and further confirmed the homogeneous dispersion of the NiCo alloy in N, O-rich graphitized carbon layers (Fig. 1(e)).

The XRD results of NiCo@NOGC, NiFe@NOGC and CoFe@NOGC are shown in Fig. 2(a) and S2.† Fig. 2(a) indicates three significant diffraction peaks at 26°, 44.38°, and 51.68°, which can be attributed to the (002) crystal planes of graphitic carbon (PDF#12-212), and (111) and (200) crystal planes of metallic Ni (PDF#01-1258) or metallic Co (PDF#01-1255), respectively. These results further confirmed the formation of NiCo alloy nanoparticles in the N, O co-doped graphitized carbon structure. Furthermore, the two strong diffraction peaks of CoFe@NOGC at 44.62° and 65.24° can be indexed to the (110) and (200) crystal planes of the CoFe alloy (PDF#00-44-1433) (Fig. S2(a)†), while NiFe@NOGC exhibits diffraction peaks at 43.1° and 50.5° corresponding to the (111) and (200) planes of the NiFe alloy (PDF#00-3-1207) (Fig. S2(b)†). These results also provide evidence for the formation of CoFe and NiFe alloy nanoparticles in the corresponding composite. However, it can be noted that no strong carbon signal was detected in NiFe@NOGC and CoFe@NOGC, which is different from that of NiCo@NOGC (Fig. 2(a)). This phenomenon indicates that

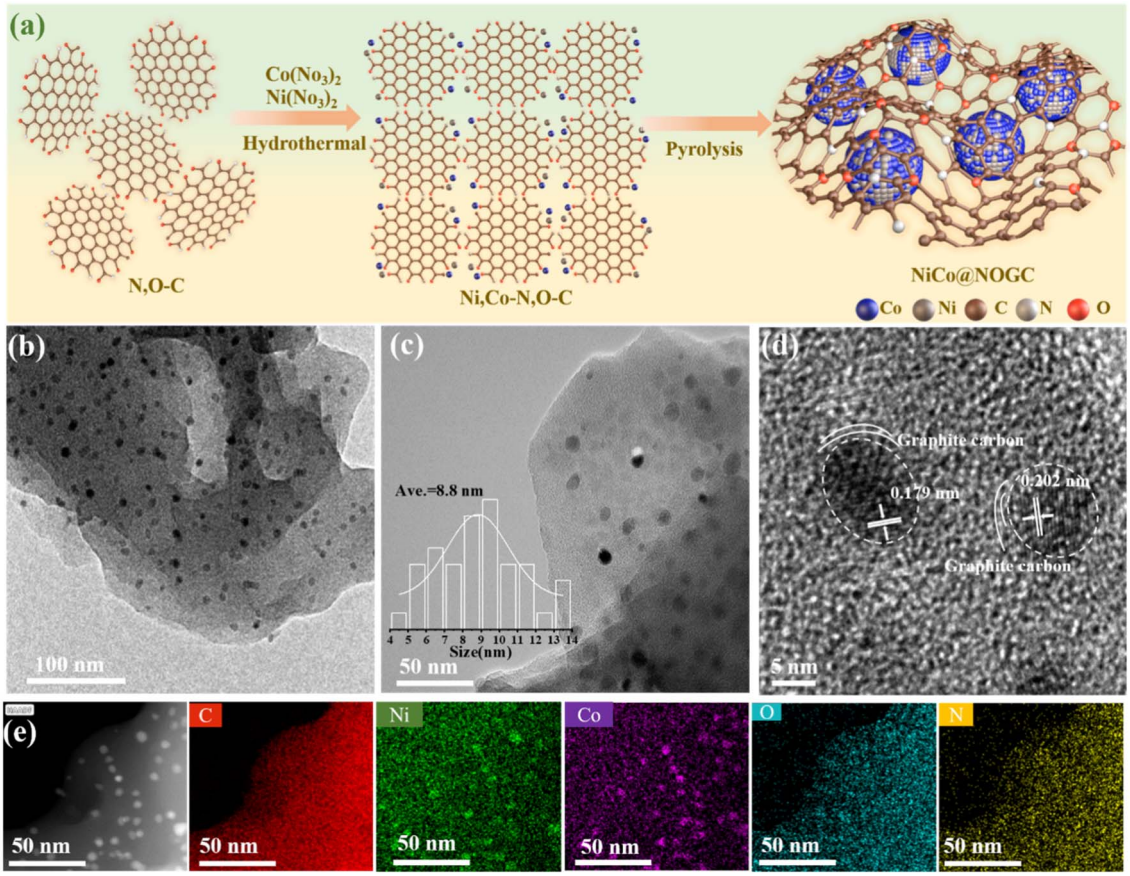

Fig. 1 Schematic diagram and characterization of the synthesized NiCo@NOGC composite. (a) Illustration of the preparation procedure of the NiCo@NOGC sample. (b–d) TEM images of the NiCo@NOGC sample with different resolutions of 100 nm (b), 50 nm (c) and 5 nm (d). (e) Elemental mapping (using EDS) of the NiCo@NOGC sample.

NiCo@NOGC has the highest graphitization degree among these three synthesized composites.

Furthermore, the Raman spectroscopy results of NiCo@NOGC (Fig. 2(b)), NiFe@NOGC and CoFe@NOGC (Fig. S3(a)†) show two typical peaks situated at 1350 and 1580 cm^{-1}, which correspond to graphitic carbon (G band) and the defect of amorphous carbon (D band), respectively. It is worth mentioning that G and D bands are related to high-frequency E_{2g} first-order graphitic crystallites and the defect-induced carbon structure, respectively.[15] The peak intensity ratios of bands G and D (I_G/I_D) of these composites were calculated to be 1.12 (NiCo@NOGC) (Fig. 2(b)), 1.07 (NiFe@NOGC) (Fig. S3(a)†), and 1.01 (CoFe@NOGC) (Fig. S3(a)†), which indicates again that the graphitization degree of NiCo@NOGC is higher than those of NiFe@NOGC and CoFe@NOGC. This indicates that the synergistic effect of metallic cobalt and nickel can promote the graphitization of carbon, thereby improving the electrochemical performance of the material. The porosities and specific surface areas of synthesized NiCo@NOGC, NiFe@NOGC, and CoFe@NOGC were measured from nitrogen adsorption/desorption isotherms (Fig. 2(d)–(e), S3(c) and (d)†). The BET surface areas of NiCo@NOGC, NiFe@NOGC, and CoFe@NOGC were estimated to be 392.9, 341.4, and 259.3 $m^2\ g^{-1}$. The enlarged surface area would facilitate the immersion of the electrolyte, and the unique porous structure effectively enhances the reaction kinetics *via* providing a large number of interfaces between electrolytes and NiCo@NOGC and reducing the ion/electron transport distance, thereby enhancing its electrochemical performance.[24]

XPS measurement was conducted to detect the chemical states and electronic structures of the surfaces of synthesized samples. XPS proved the existence of elements C, O, and N in the NiCo@NOGC sample (Fig. 2(f)). Based on XPS results, the atomic contents of O and N in NiCo@NOGC were estimated as 17.27 and 4.93%, respectively. While the low atomic contents of Co and Ni in NiCo@NOGC are about 0.43 and 0.41%, respectively. This can be attributed to that most Co and Ni are encapsulated into graphitic carbon layers, and the low Co and Ni content tested by XPS is only the surface content. However, according to the results of Inductively Coupled Plasma Optical Emission Spectrometer (ICP-OES) measurement, the exact contents of metals in the compositions are confirmed: the contents of Ni and Co in NiCo@NOGC are 3.69 and 4.28 wt%, respectively; the contents of Ni and Fe in NiFe@NOGC are 18.15 and 9.45 wt% and Co and Fe in CoFe@NOGC are 11.3 and 15.68 wt%, respectively (Table S3†). And the fitting XPS of Ni and Co is indicated in Fig S4.† And Fig. S5 and S6† indicate the XPS

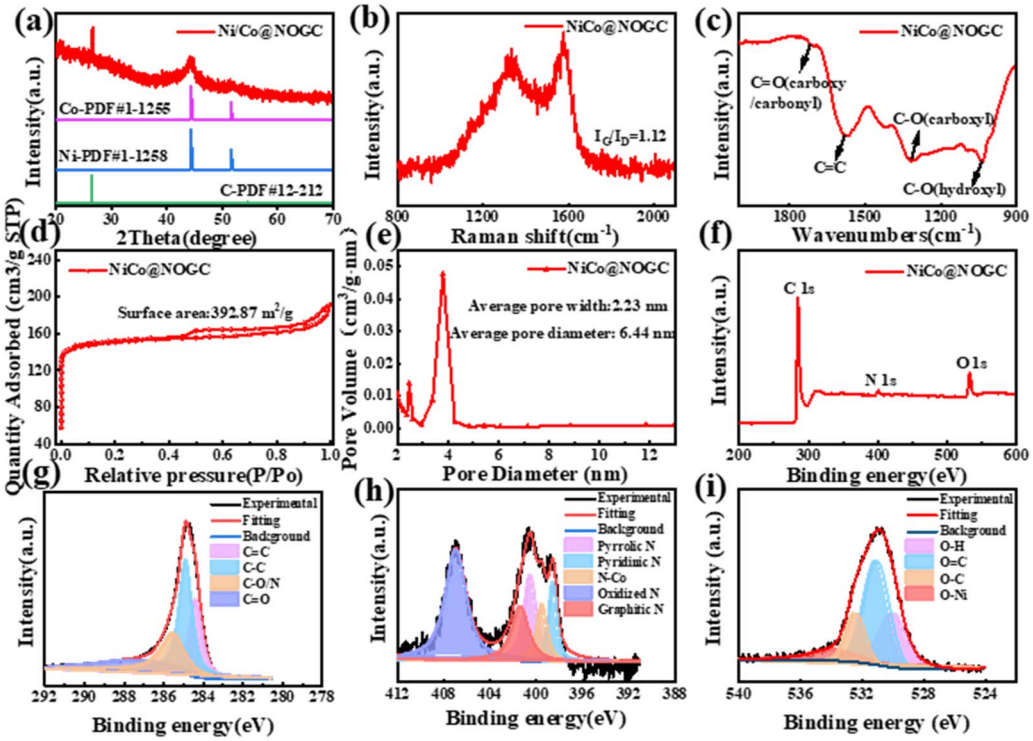

Fig. 2 Structural characterization of the synthesized NiCo@NOGC composite. (a) XRD patterns; (b) Raman spectra; (c) FTIR spectra; (d) nitrogen adsorption–desorption isotherms curve; (e) pore size distribution and (f) XPS survey spectrum; high-resolution (g) C 1s, (h) N 1s spectrum and (i) O 1s spectrum of NiCo@NOGC.

spectra of NiFe@NOGC and CoFe@NOGC composites. The detailed atomic contents of N and O of NiCo@NOGC, NiFe@NOGC, and CoFe@NOGC are listed in Table S1.† The atomic nitrogen and oxygen contents of NiCo@NOGC are higher than those of NiFe@NOGC, and CoFe@NOGC. It was confirmed by the subsequent experimental measurements and DFT calculations that high contents of nitrogen and oxygen can effectively improve the adsorption of metal K on the carbon matrix.

Fig. 2(g) shows that the spectrum of C 1s for NiCo@NOGC was fitted to four corresponding peaks at 288.7, 286.0, 284.2, and 284.7 eV, which belong to doping functional groups (C═O and C–O/N), C–C and C═C.[42,43] These data demonstrate that NiCo@NOGC was efficiently doped with oxygen and nitrogen, which agrees well with the elemental mapping results. The N 1s spectrum in Fig. 2(h) shows that five peaks of pyridinic N (398.5 eV), pyrrolic N (400.3 eV), graphitic N (401.0 eV), oxidized N (404.5 eV), and metal-bonded N (N–Co, 398.8 eV)[34,44] exist in NiCo@NOGC. Previous studies proved that pyridine and pyrrole nitrogen atoms are both lithium-philic and can be helpful to reduce nucleation overpotentials.[45] Therefore, it is highly expected that the synthesized NiCo@NOGC possesses K-philic properties to promote K nucleation. Furthermore, the O 1s spectra for NiCo@NOGC (Fig. 2(i)) can be decomposed to four peaks located at 533.0, 531.4, 532.2, and 533.9 eV, which correspond to O states for C–O, O–H, C═O, and O–Ni, respectively.[46,47] The contents of C═O, C–O and O–H were estimated as 0.46, 0.17and 0.15, respectively, by calculating their area integral. This indicates that the surface-bound oxygen is mainly in the forms of C═O and C–OH. This result can be directly supported by the FTIR measurement (Fig. 1(e) and S3(b)†) that the characteristic absorptions of carbonyl (C═O) and C–OH were clearly observed in NiCo@NOGC. In addition, the measured contents of each component of N, O functional groups by XPS analysis are listed in Table S2†. These results all show that NiCo@NOGC with rich nitrogen-oxygen functional groups was successfully synthesized.

2.2. K-philic properties of the NiCo@NOGC composite

In this section, the overpotentials of metallic K nucleation and plating were discussed and experimentally demonstrate the superiority of the synthesized NiCo@NOGC composite. Fig. 3(a) shows that two processes can be observed from the voltage–capacity curve during the potassium plating process: the sharp voltage drop at the beginning of the potassium plating process that is related to the nucleation process of metallic potassium; and the relatively stable voltage plateau that is the overpotential for mass transfer control.[45,46] The difference between the sharp tip voltage and the later stable mass transfer-controlled voltage is the nucleation overpotential (μ_n). As shown in Fig. 3(a), a sharp voltage drop to −312 mV and a μ_n of −120 mV can be observed for the bare Cu electrode during the K nucleation process. In contrast, the curve of the NiCo@NOGC electrode exhibits the smoothest voltage drop during the nucleation stage with a μ_n of only −17 mV. The measured nucleation overpotentials for NiFe@NOGC and CoFe@NOGC anodes are −35 mV and −18 mV, respectively. This can be attributed to the

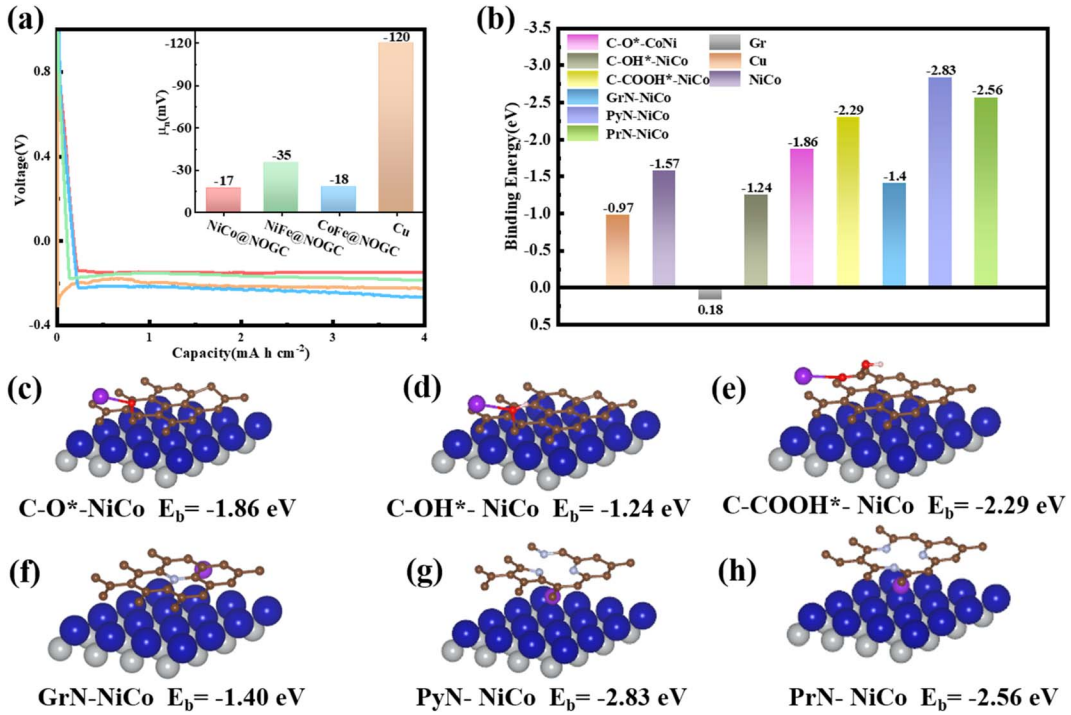

Fig. 3 Experimental and theoretical characterization of the K atom upon different surfaces. (a) The voltage–time curves during K nucleation at 0.5 mA cm^{-2} on Cu, NiCo@NOGC, NiFe@NOGC and CoFe@NOGC; (b) binding energies of a K atom with Cu and pristine and modified NiCo@NOGC surfaces; (c–h) optimized configurations for the interaction between a K atom and different modified NiCo@NOGC. Potassium, carbon, oxygen, nitrogen, nickel, and cobalt atoms in (c–h) are represented by purple, brown, red, light purple, grey and blue balls, respectively.

abundant K-philic oxygen- and nitrogen-containing functional groups on NiCo@NOGC, which facilitate the K nucleation and plating process.

To further elucidate the influence of oxygen-containing functional groups and different types of nitrogen doping on K plating, adsorption energy and charge density transfer between K atoms and different sites on NiCo@NOGC were explored by performing DFT calculations. The adsorption of K atoms on the surfaces of Cu, graphene (Gr) and the graphene/NiCo heterostructure (C–NiCo) was also studied for comparison. The calculated adsorption energies of the K atom on different surfaces are shown in Fig. 3(b) and S7(a).† The calculations of charge density difference for the adsorption of K atoms on graphene with different functional groups (Fig. S7(c)–(h)†) revealed that not only the adsorption of the K atom on graphene can be enhanced by the introduction of functional groups, but also a net gain of charge can be observed in the K atom, indicating the transfer of charge from the adsorbed K to the nearest adjacent atom. The charge depletion of the absorbed K atom and the charge accumulation around the nitrogen, oxygen-containing group were explicitly observed, suggesting a stronger K-adsorption of nitrogen, oxygen-containing functional groups on the surface. Therefore, it is highly expected to achieve a low nucleation barrier and thus a uniform deposition of K metal.

Fig. 3(b) shows that the calculated adsorption energies of the K atom and Cu (−0.97 eV) and Gr (0.18 eV) are higher than that on the NiCo surface (−1.57 eV), indicating that NiCo is more potassiophilic than Cu and graphene is an anode material. In addition, the adsorption energy between the K atom and C–NiCo heterostructure (E_b = −0.62 eV) is enhanced compared with Gr (0.18 eV) (Fig. S7(b)†). More importantly, with the introduction of COOH* (−2.29 eV), O* (−1.86 eV), and OH* (−1.24 eV) functional groups, the binding energies between the K atom and C–NiCo surfaces were enhanced (Fig. 3(c)–(e)). Hence, one can conclude that all oxygen-containing functional groups (–COOH*, –O*and –OH*) can enhance the potassium affinity of the carbon surface and are conducive to the uniform distribution of potassium ions. For nitrogen-containing functional groups, some previous studies have suggested that both pyridinic and pyrrolic nitrogen contribute to lowering the nucleation overpotential and smoothing Li plating because they are lithiophilic.[34,48] We also obtain a similar result that the binding energy between the K atom and PyN and PrN modified graphene was enhanced, indicating that pyrrolic and pyridinic nitrogen atoms can promote the deposition of K atoms. It is notable that NiCo nanoparticles of the synthesized NiCo@NOGC are uniformly embedded in graphite carbon layers surrounded by nitrogen atoms in this work (as depicted in Fig. 1(d)). Therefore, the NiCo atoms embedded in N-doping graphitic carbon layers can be directly involved in the bonding process of potassium. To prove the above analysis, the binding energies of K with NiCo@NOGC surfaces modified by GrN-NiCo (Fig. 3(f)), PyN-NiCo (Fig. 3(g)), PrN-NiCo (Fig. 3(h)) functional groups were calculated to be −1.40 eV, −2.83 eV and −2.56 eV, respectively. One can see that the binding interactions between the K atom and N-

doped graphene were significantly enhanced by the involvement of NiCo and further improved the potassiophilicity.

Furthermore, Bader charge analysis and charge density difference caculations were conducted to reveal the charge transfer during K nucleation at doping sites of NiCo@NOGC (Fig. S8†). One can see that there is no significant charge transfer between the carbon matrix and NiCo alloy during the adsorption of the K atom on the modified C–NiCo surfaces with different functional groups. However, there is a significant charge transfer from the adsorbed K atom to the N and O dopants, indicating strong chemical interactions. Furthermore, all N and O atoms form σ bonds with adjacent carbon atoms and withdraw electrons from carbon atoms due to their greater electronegativity than carbon. In addition, both N and O atoms can participate in the delocalized π system of graphene, which further enhances their negative charge state. Therefore, the abundant N, O-containing functional groups on the surface of NiCo@NOGC generate strong potassium affinity, leading to uniform K deposition. These results are also consistent with the charge analysis of the potassiophilic heteroatom-doped carbon material reported by Zhang *et al.* and Xu *et al.*[49,50] The combined results of these experiments and calculations indicate that these introduced oxygen groups and nitrogen doping enhance the K-philicity of the NiCo@NOGC surface and favour the electrochemical activity of NiCo@NOGC.

2.3. Electrochemical performance of symmetric and asymmetrical batteries

Experiments and DFT calculations in the above sections demonstrated that the NiCo@NOGC composite has favorable adsorption behavior for potassium because of the synergistic effect of NiCo nanoparticles and functional groups. Therefore, we assembled asymmetrical (NiCo@NOGC||K, NiFe@NOGC||K, CoFe@NOGC||K and Cu||K) and symmetrical cells (K–NiCo@NOGC||K–NiCo@NOGC, K–NiFe@NOGC||K–NiFe@NOGC, K–CoFe@NOGC||K–CoFe@NOGC and K–Cu||K–Cu) and their electrochemical stability was further evaluated by observing the voltage hysteresis of the time–voltage curves at different current densities and capacities. Fig. 4(a) shows that the K–NiCo@NOGC symmetrical cell delivers a lower nucleation overpotential compared to K–Cu, K–NiFe@NOGC, and K–CoFe@NOGC symmetrical cells at the current density of 0.2 mA cm^{-2}. One can see that the K–Cu symmetric cell was short-circuited after about 100 h of cycling due to the separator

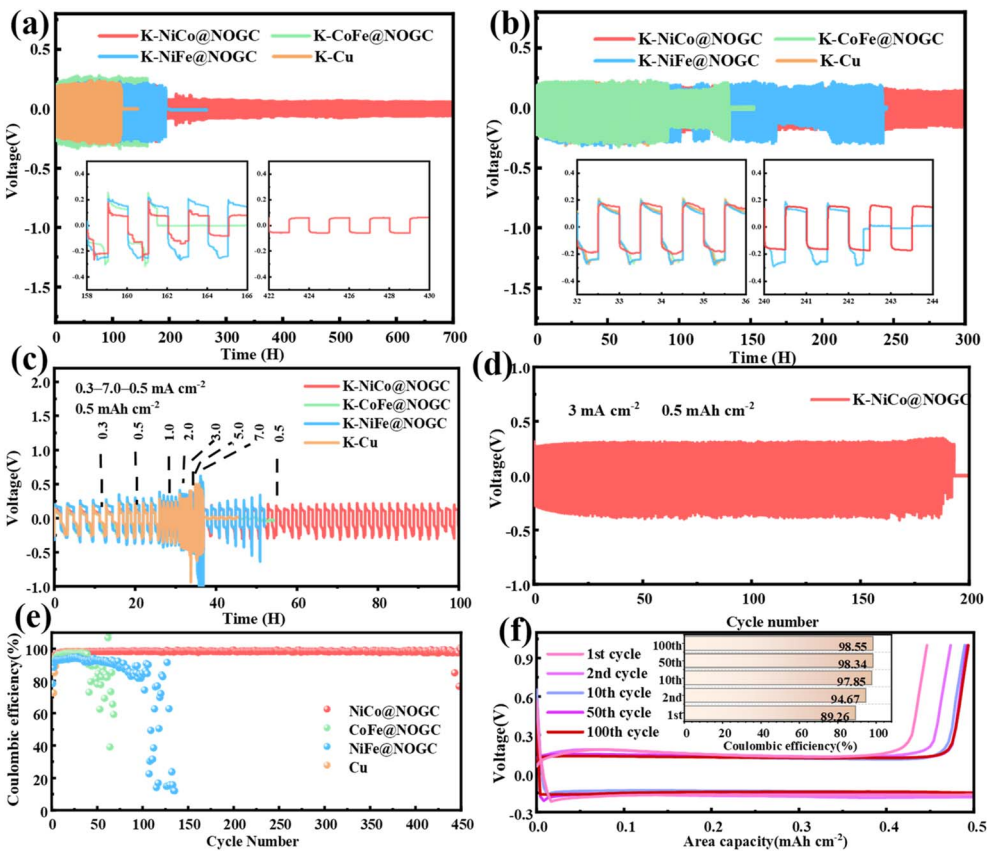

Fig. 4 Electrochemical performance of as-synthesized K metal anodes. Voltage profiles of K–NiCo@NOGC, K–NiFe@NOGC, K–CoFe@NOGC and K–Cu symmetrical cells under the conditions of (a) a current density of 0.2 mA cm^{-2} and an areal capacity of 0.2 mA h cm^{-2}, and (b) a current density of 0.4 mA cm^{-2} with a fixed cycling capacity of 0.2 mA h cm^{-2}; (c) rate performance test at current densities of 0.3 mA cm^{-2} to 7.0 mA cm^{-2} and an areal capacity of 0.5 mA h cm^{-2}; (d) voltage profiles of the K–NiCo@NOGC symmetrical cell at a high current density of 3 mA cm^{-2} with a fixed cycling capacity of 0.5 mA h cm^{-2}; (e) coulombic efficiencies of NiCo@NOGC, NiFe@NOGC, CoFe@NOGC and Cu asymmetrical cells with a K deposition amount of 0.5 mA h cm^{-2} at 0.5 mA cm^{-2}; (f) voltage profiles of the NiCo@NOGC asymmetrical cell.

pierced by the growth of dendrites. Meanwhile, although the overpotentials of K–NiFe@NOGC and K–CoFe@NOGC symmetrical cells are lower than that of the K–Cu symmetric cell, a short circuit still occurs after about 160 h and 190 h, respectively. The cause of the short circuit is still the formation of K dendrites. Surprisingly, the synthesized K–NiCo@NOGC symmetrical cell exhibited stability over 700 h with a low overpotential of ~0.07 V. Moreover, under the test conditions of a current density of 0.1 mA cm^{-2} and an areal capacity of 0.1 mA h cm^{-2}, the K–NiCo@NOGC symmetrical cell can provide an ultralong cycle stability for 1400 h (Fig. S9†). Furthermore, when the current density increases to 0.4 mA cm^{-2}, the K–NiCo@NOGC symmetrical cell still exhibits the smallest overpotential and the longest cycling stability compared with K–Cu, K–NiFe@NOGC, and K–CoFe@NOGC symmetrical cells as shown in Fig. 4(b). The K–Cu, K–NiFe@NOGC, and K–CoFe@NOGC symmetrical cells exhibited overvoltages of ~0.21, 0.20, and 0.23 V, and cycle life times of 80, 240, and 143 h, respectively. In contrast, the K–NiCo@NOGC symmetrical cell displayed an obvious protection effect and ultra-low overvoltage of only ~0.16 V for more than 300 h, proving beyond any doubt the stable interface properties of the K–NiCo@NOGC electrode during repeated K plating/stripping. Moreover, the K–NiCo@NOGC symmetric cell exhibits excellent rate performance with a steadily increased voltage hysteresis (Fig. 4(c)). When the current density is changed from 0.3 mA cm^{-2} to 0.5, 1, 2, 3, 5 and 7 mA cm^{-2}, the corresponding voltage hysteresis produced by the K–NiCo@NOGC symmetrical cell is 0.1, 0.11, 0.23, 0.27, 0.33, 0.39 and 0.41 V, respectively. As the current density recovered to 0.5 mA cm^{-2}, the K–NiCo@NOGC symmetrical cell could still work stably for more than 100 hours, but K–Cu, K–NiFe@NOGC, and K–CoFe@NOGC symmetrical cells failed in a short time. Furthermore, when the K–NiCo@NOGC symmetrical cell is tested under conditions of a current density of 0.5 mA cm^{-2} and areal capacity of 0.5 mA h cm^{-2}, it can still provide stable cycling for more than 250 h (Fig S10†). Even when the high current density increases to 3.0 mA cm^{-2}, the K–NiCo@NOGC symmetric cell maintains stable cycling stability with an over-potential of about 0.31 V for nearly 200 cycles (Fig. 4(d)). The excellent cycling performance of the NiCo@NOGC electrode further demonstrates that the strong K-philic matrix favors uniform deposition of K and enables ultra-stable cycling performance.

Coulombic efficiency (CE), defined as the ratio of stripping to plating capacity per cycle, is an important metric for evaluating the reversibility of K metal anodes. Therefore, to test the reversibility of each synthesized K metal anode during the repeated process of plating/stripping, the CEs on NiCo@NOGC, NiFe@NOGC, CoFe@NOGC and Cu asymmetrical cells were tested under the conditions of a current density of 0.5 mA cm^{-2} and an areal capacity of 0.5 mA h cm^{-2} (Fig. 4(e)). The Cu asymmetrical cell only lasts about 30 cycles before being shorted. Owing to the large specific surface area and abundant potassium adsorption sites, the NiFe@NOGC, CoFe@NOGC, and NiCo@NOGC electrodes can facilitate uniform current density and provide space for deposition of K during cycling. Therefore, compared with the Cu asymmetrical cell, the NiFe@NOGC and CoFe@NOGC asymmetrical cells provide 92.0% and 96.0% stable CE after nearly 60 and 90 cycles, respectively. Remarkably, one can see that the NiCo@NOGC asymmetrical cell exhibits a higher CE of 99.4% at 450 cycles and the full voltage–time curve of the NiCo@NOGC asymmetrical cell is shown in Fig. S11.† Fig. 4(f) shows that the coulombic efficiency continues to increase with the increase of the number of cycles. Moreover, the NiCo@NOGC matrix also exhibits high and stable average CEs of 93.1% and 91.5% at high current densities of 1.0 and 2.0 mA cm^{-2}, respectively (Fig. S12†). A high CE is beneficial to the formation of a stable and homogeneous SEI on the electrode. In addition, X-ray photoelectron spectroscopy (XPS) measurements were performed to examine the chemical information of SEI layers on the cycled Cu–K and NiCo@NOGC-K anodes (Fig. S13†). The relative amount of carbon species is higher in the SEI on the cycled Cu–K (38.6%) than that on the cycled NiCo@NOGC-K (12.7%). Because the organic species is based on carbon, the higher C content indicates more organic components in the SEI, which is attributed to the continuous reaction between the K metal and the electrolyte. Therefore, such a stable and uniform SEI on the surface of the NiCo@NOGC-K composite electrode is beneficial to fast K ion migration and guarantees reversible K plating/stripping. Furthermore, the superiority of the K–NiCo@NOGC symmetrical cell was also demonstrated by electrochemical impedance spectroscopy (EIS) analysis. We know that the high-frequency semicircle radius in the Nyquist plots is related to the charge transfer resistance and the SEI resistance.[51,52] Before cycling, the interfacial resistance of the K–NiCo@NOGC symmetric cell is the smallest compared with the K–CoFe@NOGC, K–NiCo@NOGC and K–Cu symmetric cells (Fig. S14†). More importantly, the interfacial resistance of the NiCo@NOGC symmetric cell decreases with increasing cycle times, further indicating a more stable SEI with less exposure of potassium to the electrolyte.

2.4. K plating and stripping behavior of asymmetric cells

The excellent electrochemical performance indicates that the NiCo@NOGC electrode is highly reversible. It is well known that uniform K nucleation and deposition behaviors can effectively improve the reversibility of K metal anodes during cycling. Therefore, the excellent cycling and CE performances of NiCo@NOGC asymmetric cells are attributed to the strong potassiophility of the NiCo@NOGC matrix, which can promote uniform nucleation behavior while reducing the nucleation overpotential. To confirm this mechanism, *ex situ* SEM tests were performed to characterize the morphology evolution and dendrite growth shape of Cu, NiCo@NOGC, NiFe@NOGC, and CoFe@NOGC asymmetric cells after potassium deposition/stripping at a constant current of 0.5 mA cm^{-2} before K plating, and all assembled coin cells were activated for five cycles in the potential range of 0.01–1.0 V at a current density of 50 μA cm^{-2} before K plating to form stable SEI films (Fig. S15†).

The SEM images of Cu, NiCo@NOGC, NiFe@NOGC, and CoFe@NOGC electrodes before and after K plating are shown in Fig. 5 and S16.† Compared with the original Cu foil electrode

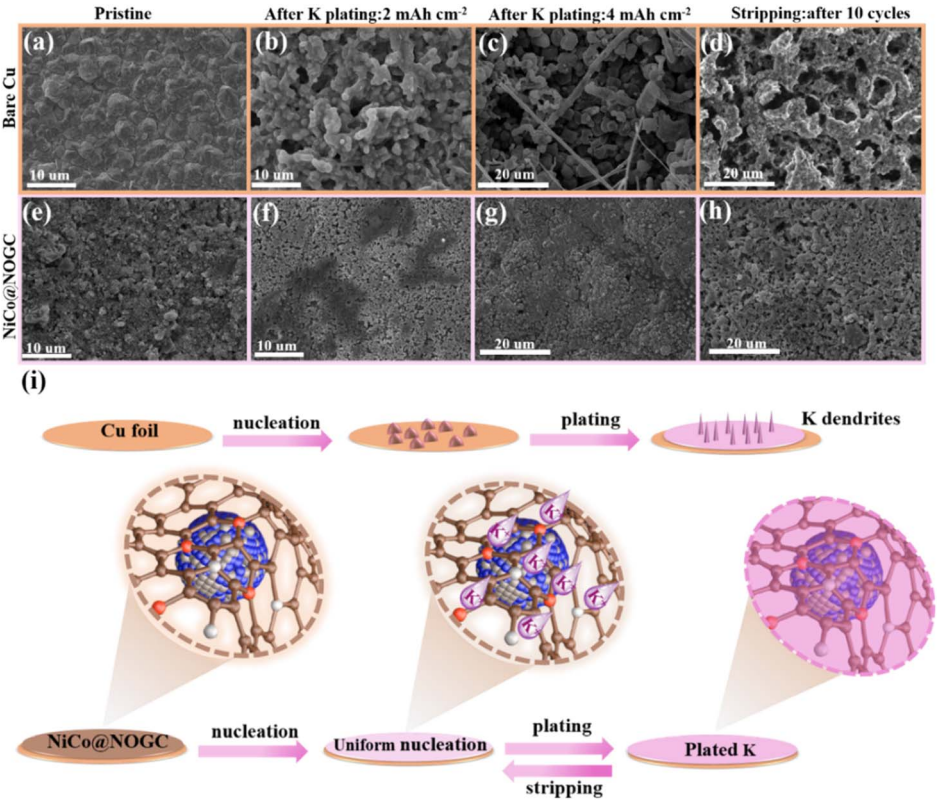

Fig. 5 Morphology evolution of Cu and NiCo@NOGC electrodes during plating/stripping. (a–d) SEM images of (a) Cu and (e) NiCo@NOGC electrodes before K plating; (b) Cu and (f) NiCo@NOGC after plating at 2 mA h cm^{-2}; (c) Cu and (g) NiCo@NOGC after plating at 4 mA h cm^{-2}; (d) Cu and (h) NiCo@NOGC after 10 cycles of stripping at 0.5 mA cm^{-2}; (i) schematic illustration of the K plating/stripping behaviours on Cu foil and NiCo@NOGC.

(Fig. 5(a)), the surface of the Cu foil electrode after plating at a discharge capacity of 2 mA h cm^{-2} is covered with a few rod-like K nucleation particles (Fig. 5(b)). After plating at a capacity of 4 mA h cm^{-2}, it becomes a porous structure with growth of dendrites (Fig. 5(c)). This porous electrode produces an inhomogeneous K flux, leading to inhomogeneous K plating and dendrite formation in subsequent cycles.[53-55] As a result, large K protrusions can be observed on the bare Cu electrode after 10 cycles of plating/stripping (Fig. 5(d)). In addition, morphology evolution of NiFe@NOGC and CoFe@NOGC electrodes is shown in Fig. S16.† Compared with the initial stage of K plating (Fig. S16(a) and (e)†), the surfaces of the NiFe@NOGC and CoFe@NOGC electrodes exhibit rod-like structures after plating at a capacity of 2 mA h cm^{-2} (Fig. S16(b) and (f)†), and with K deposition increased at a capacity of 4 mA h cm^{-2} (Fig. S16(c) and (g)†), the surface of the NiFe@NOGC and CoFe@NOGC electrodes became relatively flat but not dense. Meanwhile, after 10 cycles of K plating/stripping (Fig. S16(d) and (h)†), the surfaces of NiFe@NOGC and CoFe@NOGC electrodes also show a relatively flat but not dense surface with some small potassium nanoparticles. In sharp contrast, both at the initial stage of K plating (Fig. 5(e)) and at the total capacity of 2 mA h cm^{-2} (Fig. 5(f)) and 4 mA h cm^{-2} (Fig. 5(g)) for successive K deposition, the NiCo@NOGC electrode shows a relatively smooth surface without any protruding rods. In particular, these smooth and flat potassium deposits are mainly accommodated in the pores around the NiCo particles. All these results further suggest that surface functional groups can guide the nucleation of K for uniform distribution, thus avoiding the formation of K dendrites at NiCo@NOGC electrodes. Furthermore, after plating/stripping of 10 cycles (Fig. 5(h)), the NiCo@NOGC electrode still indicates a smooth surface without any dendrite shape because of the suppressed volume change, which is beneficial to guarantee a stable and uniform SEI. The TEM and HRTEM measurements and elemental mapping of the NiCo@NOGC electrode were further carried out after plating/stripping for 10 cycles at 0.5 mA cm^{-2} at an areal capacity of 0.5 mA h cm^{-2}. As shown in Fig. S17,† the morphology of NiCo nanoparticles was not changed and the nanoparticles are still uniformly dispersed in N- and O-rich 2D graphited carbon layers. Moreover, the average size of NiCo alloy nanoparticles after plating/stripping for 10 cycles (9.03 nm) was slightly changed significantly compared to that before cycling (8.8 nm), which further validates the high structural stability of NiCo@NOGC during cycling. The corresponding mapping exhibits a uniform element distribution, with K metal first nucleating at highly potassiophilic sites and embedded in the carbon matrix. These results demonstrated that the NiCo@NOGC electrode can achieve uniform K plating/stripping without the formation of potassium dendrites, leading to highly stable electrodes and

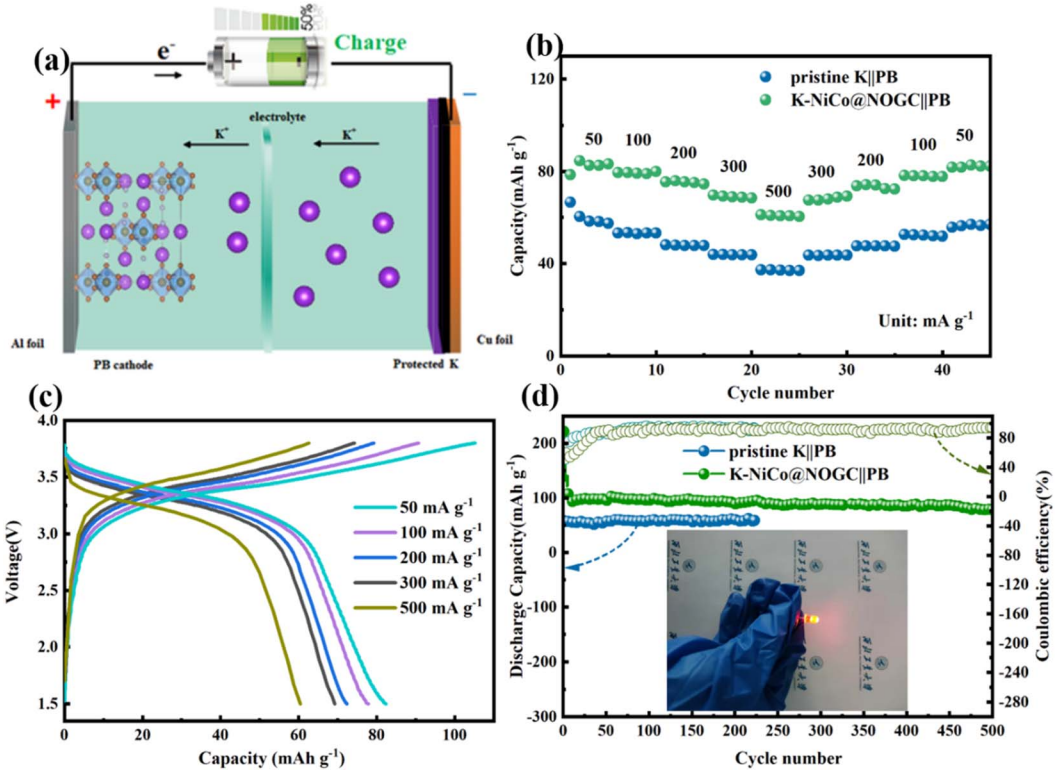

Fig. 6 Electrochemical performance of the synthesized full cells. (a) Schematic illustration of the K–NiCo@NOGC||PB cell; (b) rate performance of K–NiCo@NOGC||PB and pristine K ||PB cells; (c) charge/discharge profiles of K–NiCo@NOGC||PB cells; (d) cycling performance of K–NiCo@NOGC||PB and pristine K ||PB cells at 50 mA g^{-1}.

interfaces in working cells. Fig. 5(i) schematically illustrates the mechanism of K deposition on NiCo@NOGC without dendrites after repeated cycling. This is of great significance for improving the cycle performance of potassium metal batteries.

2.5. Performance of the K–NiCo@NOGC anode in full cells

In the above sections, it is demonstrated that the NiCo@NOGC matrix exhibits excellent electrochemical performances as an anode for PMBs due to its strong K metal affinity. To further demonstrate its potential application for PIBs, K metal full cells, named K–NiCo@NOGC||PB, were assembled with K–NiCo@NOGC as the anode material and Prussian blue (PB) as the cathode material (as illustrated in Fig. 6(a)). For comparison, we also assembled pristine K||PB batteries (pristine K as the anode and Prussian blue (PB) as the cathode material). These full cells with a carbonate-based electrolyte were employed in the voltage range of 1.5–3.8 V. The synthesis of PB was evidenced by the XRD pattern of PB (Fig. S18(a)†) and the CV curves of PB at a scan rate of 0.2 mV s^{-1} (Fig. S18(b)†). The rate performances of these assembled full batteries at different current densities were tested. As shown in Fig. 6(b), compared with the pristine K||PB full battery, an enhanced rate capability is obtained for the K–NiCo@NOGC||PB full battery with a higher discharge capacity of 84.7, 79.5, 75.9, 69.2 and 60.9 mA h g^{-1} at a current density of 50, 100, 200, 300, and 500 mA g^{-1}, respectively. Fig. 6(c) and S19† show the charge–discharge curves and specific capacity of K–NiCo@NOGC||PB pristine K||PB batteries at different current densities, which imply that K–NiCo@NOGC can greatly increase the capacity of the full battery and without reducing the voltage platform. Fig. 6(d) compares the cycling stability of the batteries assembled with the NiCo@NOGC and pure potassium anodes at 50 mA g^{-1}. The pristine K||PB full cells indicates a low specific capacity of 58 mA h g^{-1} after 200 cycles. However, the K–NiCo@NOGC||PB full battery delivers a high reversible specific capacity of 80 mA h g^{-1} and 80% capacity retention after 500 cycles. In addition, an LED bulb was lit by one K–NiCo@NOGC||PB full battery. These results all demonstrate that the potassiophilic NiCo@NOGC matrix can enable a high utilization of K metal during cycling by decreasing the depletion of irreversible K. Meanwhile, these results fully demonstrate that the uniform and stable deposition behavior of K on NiCo@NOGC substrates can effectively improve the electrochemical properties of potassium metal batteries.

3 Conclusions

In this work, a N, O co-doped 2D graphited carbon matrix with embedded binary-metal (NiCo, NiFe and CoFe) nanoparticles was synthesized with abundant functional groups evenly distributed on the surface. It is worth noting that the NiCo@NOGC matrix was successfully adopted to realize an excellent potassium metal anode by coating it on Cu foil. DFT calculation results revealed that the O and N-containing functional groups of NiCo@NOGC significantly enhance the affinity

of the NiCo@NOGC matrix for K, thereby promoting the uniform deposition behavior of K without dendrite formation. Experimental results show that the NiCo@NOGC matrix can serve as an excellent host for the K metal anode with a high coulombic efficiency of 99.4% after 450 cycles at 0.5 mA cm^{-2} and stable cycling for 1400 h in a symmetric cell at a current density of 0.1 mA cm^{-2} and an areal capacity of 0.1 mA h cm^{-2}. Moreover, the full battery assembled based on the K–NiCo@NOGC metal anode and PB cathode exhibits excellent cycling performance. The successful strategy of this study opens a prospect for designing high-energy-density K secondary batteries using the K metal anode and shows great potential in energy storage applications.

Conflicts of interest

There are no conflicts to declare.

Acknowledgements

This work was financially supported by the National Nature Science Foundation of China (Grant No. 52272307 and 52111530033) and the Fundamental Research Funds for the Central Universities (No. D5000220172).

Notes and references

1 Q. Sun, Z. Cao, Z. Ma, J. Zhang, H. Cheng, X. Guo, G.-T. Park, Q. Li, E. Xie, L. Cavallo, Y.-K. Sun and J. Ming, *ACS Energy Lett.*, 2022, **7**, 3545–3556.
2 Z. Liu, S. Chu, J. Wu, C. Cheng, L. Zhang, S. Guo and H. Zhou, *Chem. Eng. J.*, 2022, **435**, 134944.
3 J. Li, J. Song, L. Luo, H. Zhang, J. Feng, X. Zhao, X. Guo, H. Dong, S. Chen, H. Liu, G. Shao, T. D. Anthopoulos, Y. Su, F. Wang and G. Wang, *Adv. Energy Mater.*, 2022, **12**(32), 2200894.
4 Y. Fang, Y. Zeng, Q. Jin, X. F. Lu, D. Luan, X. Zhang and X. W. D. Lou, *Angew. Chem., Int. Ed. Engl.*, 2021, **60**, 8515–8520.
5 Y. Gao, Z. Hou, R. Zhou, D. Wang, X. Guo, Y. Zhu and B. Zhang, *Adv. Funct. Mater.*, 2022, **32**(17), 2112399.
6 C. Liu, Q. Yin, Y. Liu, K. Xu, N. Zhao, C. Lao, J. Shen and Z. Chen, *J. Adv. Ceram.*, 2022, **11**, 295–307.
7 K. Yuan, T. Tu, C. Shen, L. Zhou, J. Liu, J. Li, K. Xie and G. Zhang, *J. Adv. Ceram.*, 2022, **11**, 882–892.
8 B. Dunn, H. Kamath and J.-M. Tarascon, *Science*, 2011, **334**, 928–935.
9 X. Ji, Y. Zhang, M. Cao, Q. Gu, H. Wang, J. Yu, Z.-H. Guo and X. Zhou, *J. Adv. Ceram.*, 2022, **11**, 835–861.
10 X. Wu, X. Liang, X. Zhang, L. Lan, S. Li and Q. Gai, *J. Adv. Ceram.*, 2021, **10**, 347–354.
11 J. Meng, H. Zhu, Z. Xiao, X. Zhang, C. Niu, Y. Liu, G. Jiang, X. Wang, F. Qiao, X. Hong, F. Liu, Q. Pang and L. Mai, *ACS Nano*, 2022, **16**, 7291–7300.
12 S. Lee, H. Park, J. Rizell, U. H. Kim, Y. Liu, X. Xu, S. Xiong, A. Matic, A. T. Zikri, H. Kang, Y. K. Sun, J. Kim and J. Y. Hwang, *Adv. Funct. Mater.*, 2022, **32**(46), 2209145.
13 L. Cui, Z. Wang, S. Kang, Y. Fang, Y. Chen, W. Gao, Z. Zhang, X. Gao, C. Song, X. Chen, Y. Wang and G. Wang, *ACS Appl. Mater. Interfaces*, 2022, **14**, 12551–12561.
14 P. Liu, H. Hao, H. Celio, J. Cui, M. Ren, Y. Wang, H. Dong, A. R. Chowdhury, T. Hutter, F. A. Perras, J. Nanda, J. Watt and D. Mitlin, *Adv. Mater.*, 2022, **34**, e2105855.
15 Q. Shen, P. Jiang, H. He, C. Chen, Y. Liu and M. Zhang, *Nanoscale*, 2019, **11**, 13511–13520.
16 J. Hao, H. Xia, A. M. Rao, Y. He, J. Zhou and B. Lu, *Energy Storage Mater.*, 2022, **53**, 148–155.
17 Z. Tai, Y. Li, Y. Liu, L. Zhao, Y. Ding, Z. Lu, Z. Peng, L. Meng, G. Yu and L. Liu, *Adv. Sci.*, 2021, **8**, e2101866.
18 J. Wang, W. Yan and J. Zhang, *Nano Energy*, 2022, **96**, 107131.
19 P. Liu, H. Hao, H. Celio, J. Cui, M. Ren, Y. Wang, H. Dong, A. R. Chowdhury, T. Hutter, F. A. Perras, J. Nanda, J. Watt and D. Mitlin, *Adv. Mater.*, 2022, **34**, 2105855.
20 Z. Wei, A. Wang, X. Guan, G. Li, Z. Yang, C. Huang, J. Zhang, L. Ren, J. Luo and X. Liu, *Energy Environ. Mater.*, 2022, **5**, 1278–1284.
21 A. Eftekhari, Z. Jian and X. Ji, *ACS Appl. Mater. Interfaces*, 2016, **9**, 4404–4419.
22 Y. Ding, X. Guo, Y. Qian, H. Gao, D. H. Weber, L. Zhang, J. B. Goodenough and G. Yu, *Angew. Chem., Int. Ed.*, 2020, **59**, 12170–12177.
23 J. Zhang, Y. Li, L. Zhu, X. Wang and J. Tu, *Energy Storage Mater.*, 2021, **41**, 606–613.
24 L. Wang, H. Wang, M. Cheng, Y. Hong, M. Li, H. Su, J. Sun, J. Wang and Y. Xu, *ACS Appl. Energy Mater.*, 2021, **4**, 6245–6252.
25 N. Xiao, W. D. McCulloch and Y. Wu, *J. Am. Chem. Soc.*, 2017, **139**, 9475–9478.
26 B. Ji, F. Zhang, X. Song and Y. Tang, *Adv. Mater.*, 2017, **29**, 1700519.
27 W. Xu, H. Wang, J. Hu, H. Zhang, B. Zhang, F. Kang and D. Zhai, *Chem. Commun.*, 2021, **57**, 1034–1037.
28 Y. Hu, L. Fan, A. M. Rao, W. Yu, C. Zhuoma, Y. Feng, Z. Qin, J. Zhou and B. Lu, *Natl. Sci. Rev.*, 2022, **9**, nwac134.
29 Y. Zhang, A. Bahi, F. Ko and J. Liu, *Small*, 2022, **18**, e2107186.
30 W. Yuan, Y. Li, T. Ding, L. Zhang and J. Shu, *Chem. Eng. J.*, 2022, **432**, 134353.
31 D. Lin, Y. Liu, Z. Liang, H.-W. Lee, J. Sun, H. Wang, K. Yan, J. Xie and Y. Cui, *Nat. Nanotechnol.*, 2016, **11**, 626–632.
32 L. Liu, Y.-X. Yin, J.-Y. Li, N.-W. Li, X.-X. Zeng, H. Ye, Y.-G. Guo and L.-J. Wan, *Joule*, 2017, **1**, 563–575.
33 H. Shi, M. Yue, C. J. Zhang, Y. Dong, P. Lu, S. Zheng, H. Huang, J. Chen, P. Wen, Z. Xu, Q. Zheng, X. Li, Y. Yu and Z.-S. Wu, *ACS Nano*, 2020, **14**, 8678–8688.
34 Z. Guo, F. Wang, Z. Li, Y. Yang, A. G. Tamirat, H. Qi, J. Han, W. Li, L. Wang and S. Feng, *J. Mater. Chem. A*, 2018, **6**, 22096–22105.
35 R. Jiang, W. Diao, D. Xie, F. Tao, X. Wu, H. Sun, W. Li and J. Zhang, *ACS Appl. Energy Mater.*, 2021, **4**, 12871–12881.
36 G. Xiao, W. Cai, L. Zhu, Y. Fang, H. Ao, Y. Zhu and Y. Qian, *Inorg. Chem. Front.*, 2020, **7**, 2747–2752.
37 P. Zhai, T. Wang, W. Yang, S. Cui, P. Zhang, A. Nie, Q. Zhang and Y. Gong, *Adv. Energy Mater.*, 2019, **9**, 1804019.

38 L. Yao, Q. Wu, P. Zhang, J. Zhang, D. Wang, Y. Li, X. Ren, H. Mi, L. Deng and Z. Zheng, *Adv. Mater.*, 2018, **30**(11), 1706054.
39 J. Qin, T. Wang, D. Liu, E. Liu, N. Zhao, C. Shi, F. He, L. Ma and C. He, *Adv. Mater.*, 2018, **30**, 1704670.
40 W. Li, Y. Liu, M. Wu, X. Feng, S. A. T. Redfern, Y. Shang, X. Yong, T. Feng, K. Wu, Z. Liu, B. Li, Z. Chen, J. S. Tse, S. Lu and B. Yang, *Adv. Mater.*, 2018, **30**, e1800676.
41 A. Kumar, V. Q. Bui, J. Lee, L. Wang, A. R. Jadhav, X. Liu, X. Shao, Y. Liu, J. Yu, Y. Hwang, H. T. D. Bui, S. Ajmal, M. G. Kim, S. G. Kim, G. S. Park, Y. Kawazoe and H. Lee, *Nat. Commun.*, 2021, **12**, 6766.
42 Z. Zheng, X. Zeng, H. Ye, F. Cao and Z. Wang, *ACS Appl. Mater. Interfaces*, 2018, **10**, 30417–30425.
43 Y. Xie, J. Hu, Z. Han, H. Fan, J. Xu, Y. Lai and Z. Zhang, *Nano Res.*, 2020, **13**, 3137–3141.
44 L. Lu, Y. Liu, J. Fan, L. Wang, Y. Lin, D. Xu, Z. Dai and M. Han, *Chem. Commun.*, 2020, **56**, 10010–10013.
45 R. Zhang, X. R. Chen, X. Chen, X. B. Cheng, X. Q. Zhang, C. Yan and Q. Zhang, *Angew. Chem., Int. Ed. Engl.*, 2017, **56**, 7764–7768.
46 K. Liu, Z. Li, W. Xie, J. Li, D. Rao, M. Shao, B. Zhang and M. Wei, *Energy Storage Mater.*, 2018, **15**, 308–314.
47 C. Gao, J. Li, K. Sun, H. Li, B. Hong, M. Bai, K. Zhang, Z. Zhang and Y. Lai, *Chem. Eng. J.*, 2021, **412**, 128721.
48 T.-S. Wang, X. Liu, X. Zhao, P. He, C.-W. Nan and L.-Z. Fan, *Adv. Funct. Mater.*, 2020, **30**, 2000786.
49 M. Zhou, W. Qi, Z. Hu, M. Cheng, X. Zhao, P. Xiong, H. Su, M. Li, J. Hu and Y. Xu, *ACS Appl. Mater. Interfaces*, 2021, **13**, 17629–17638.
50 X. Chen, Y.-K. Bai, X. Shen, H.-J. Peng and Q. Zhang, *J. Energy Chem.*, 2020, **51**, 1–6.
51 J. Z. Wenxiu Yang, S. Wang, W. Zhang, Z. Wang, L. Fan, K. Wang, Q. Sun and S. Guo, *Energy Environ. Sci.*, 2019, **12**, 1605–1612.
52 C. Chen, Y. Yang, S. Ding, Z. Wei, X. Tang, P. Li, T. Wang, G. Cao and M. Zhang, *Energy Storage Mater.*, 2018, **13**, 215–222.
53 X. B. Cheng, R. Zhang, C. Z. Zhao and Q. Zhang, *Chem. Rev.*, 2017, **117**, 10403–10473.
54 C. Wang, A. Wang, L. Ren, X. Guan, D. Wang, A. Dong, C. Zhang, G. Li and J. Luo, *Adv. Funct. Mater.*, 2019, **29**, 1905940.
55 S. Wang, Y. Yan, D. Xiong, G. Li, Y. Wang, F. Chen, S. Chen, B. Tian and Y. Shi, *Angew. Chem., Int. Ed. Engl.*, 2021, **60**, 25122–25127.